Cuesta, F. S.; Faniayeu, I. A.; Asadchy, V. S.; Tretyakov, S. A.

Planar broadband Huygens' metasurfaces for wave manipulations

Published in:
IEEE Transactions on Antennas and Propagation

DOI:
10.1109/TAP.2018.2869256

Published: 01/01/2018

Document Version
Peer-reviewed accepted author manuscript, also known as Final accepted manuscript or Post-print

Planar broadband Huygens' metasurfaces for wave manipulations

Francisco S. Cuesta, Ihar A. Faniayeu, Viktar S. Asadchy, and Sergei A. Tretyakov, *Fellow, IEEE*

***Abstract*—Electrically thin and effectively two-dimensional material composites, metasurfaces, have been widely exploited for manipulation of electromagnetic waves. For many applications it is desired to transform incident waves of a specific frequency range keeping the metasurface invisible at other frequencies. Such frequency-selective response can be achieved based on subwavelength Huygens' inclusions. However, their fabrication requires sophisticated processes due to the three-dimensional geometry. Here, we propose a planar Huygens' meta-atom with the goal to open a way to realize broadband invisible metasurfaces with topologies suitable for the conventional printed circuit board fabrication technology. We synthesize and analyse, both numerically and experimentally, three different metasurfaces capable of polarization and amplitude transformations of incident waves.**

***Index Terms*—Huygens; metasurface; chirality; matching; transparency.**

I. Introduction

TRANSFORMATION of electromagnetic waves is of cardinal importance for a variety of applications, including beam forming, sensing, filtering, beam steering, and others. It implies modification of one or several wave properties such as the amplitude, phase, polarization, and wavefront shape. First devices for wave transformations, mirrors and lenses, have been used since ancient times. Subsequently, the engineer's toolbox was enlarged by more advanced structures: diffraction gratings, prisms, filters, wave plates, etc. In the early twentieth century, during the heyday of microwave techniques, active and passive antenna arrays were introduced, offering rather general control of electromagnetic waves. Passive arrays are typically categorized into two groups, namely, reflectarrays [1]–[6] and transmitarrays [7], [8]. Importantly, both reflectarray and transmitarray antennas incorporate a ground plane to illuminate unwanted scattering [1]–[8]. As a result, the ground plane inevitably blocks electromagnetic radiation outside the operating frequency band of the antenna, creating a shadow. This effect is unwanted in several applications. Firstly, the antenna becomes detectable in the entire electromagnetic spectrum, which might hinder the use of the antenna for military purposes. Secondly, the antenna shadow does not allow to detect or manipulate electromagnetic waves of other frequencies behind the antenna.

Francisco S. Cuesta, Viktar S. Asadchy, and Sergei A. Tretyakov are with Department of Electronics and Nanoengineering, Aalto University, P.O. 15500, FI-00076, Aalto, Finland (e-mail: francisco.cuestasoto@aalto.fi, viktar.asadchy@aalto.fi, sergei.tretyakov@aalto.fi).

I. A. Faniayeu is with the Department of Physics, University of Gothenburg, Gothenburg 412 96, Sweden (e-mail: ihar.faniayeu@physics.gu.se).

Frequency-selective devices which transform the incident waves in the required manner within the operational band, remaining transparent at other frequencies, can open up new practical opportunities. Such broadband-transparent structures do not create unwanted blockage of radiation and cannot be detected at non-operational frequencies. Early attempts to create frequency-selective array antennas relied on the idea of replacing the ground plane by a mesh of thin metal wires. At the frequencies below the operational band the mesh efficiently emulates a ground plane. At elevated frequencies, the mesh becomes practically transparent, but still there are significant reflections [9]. In contrast, frequency selective surfaces [10] (also called FSSs) can overcome the problem of transmission blockage and possess response of a notch filter for propagating waves [11], [12]. However, FSSs cannot provide additional functionalities such as uniaxial polarization conversion and efficient beam bending since they do not possess chirality [13] (being mirror-symmetric) and do not allow full phase control over transmission and reflection.

Recent developments of metasurfaces, artificial thin composite material layers, provided a platform for novel wave-transforming devices with extended functionalities. A metasurface represents a two-dimensional array of sub-wavelength inclusions [14]–[16]. It was demonstrated that full control over normally incident waves can be achieved only when a metasurface possesses both electric and magnetic response (including so-called *Huygens'* metasurfaces) as well as magnetoelectric coupling (e.g., chirality) [13], [17]–[22]. In order to realize ideal frequency-selective response from a metasurface, i.e. exhibiting some particular functionality (such as absorption or cross-polarized reflection) at the resonance frequency and being transparent at other frequencies, it is required that the electric and effective magnetic currents flowing on the metasurface have the same amplitudes and frequency dispersions (to ensure zero reflections in a broad frequency range). Such scenario can be realized in metasurfaces formed by single-wire bianisotropic inclusions [23], [24] or pairs of electric and magnetic anisotropic inclusions with properly chosen properties [25] (the latter case is applicable only for lossless metasurfaces). Although previous designs of such metasurfaces demonstrated high efficiency of polarization control and beam deflection [23]–[28], it is a great challenge to fabricate them due to the *three-dimensional* geometry of their metallic inclusions even for microwave frequencies.

In this paper, we report on the realization of planar broadband Huygens metasurfaces based on 3D bianisotropic inclusions using conventional printed circuit board (PCB) techniques [26], [29]–[32]. The proposed metasurfaces are

fabricated as dielectric substrates with copper patterns on both their sides connected with vias (copper-plated holes that function as current channels through the dielectric substrate). The individual metasurface inclusions have mirror-asymmetric geometry to ensure general electromagnetic response as well as nearly perfect spectral matching of electric and magnetic resonances. Three different devices have been designed, namely a frequency-selective perfect absorber and two polarization rotators operating in reflection and transmission modes (in the microwave range). Both numerical and experimental results reveal broadband transparency (invisibility) for electromagnetic radiation outside the resonance band (typically from 0 Hz up to the double resonance frequency). The devices can be easily integrated in existing systems and even be cascaded for achieving multifrequency multifunctional operations.

II. Design and Characterization of the Individual Metasurface Inclusions

Our two main objectives for the design of functional broadband Huygens' metasurfaces capable of various wave transformations are the following: 1) The metasurface should be transparent for incident waves beyond the operational band, meaning that the transmission coefficient $|T| \approx 1$; 2) The metasurface should be fabrication-friendly, i.e., it can be manufactured with existing planar technologies. These objectives are illustrated in Fig. 1 where incident waves of different frequencies are shown in different colors. The waves at the operational band (green color) are fully reflected with 90° polarization rotation. *Resonant* metasurfaces consisting of single inclusions are ideal candidates for this role since, far from the resonance, they are weakly excited and create no absorption. However, near the resonance, the inclusions can create strong and controllable reflections if their properties

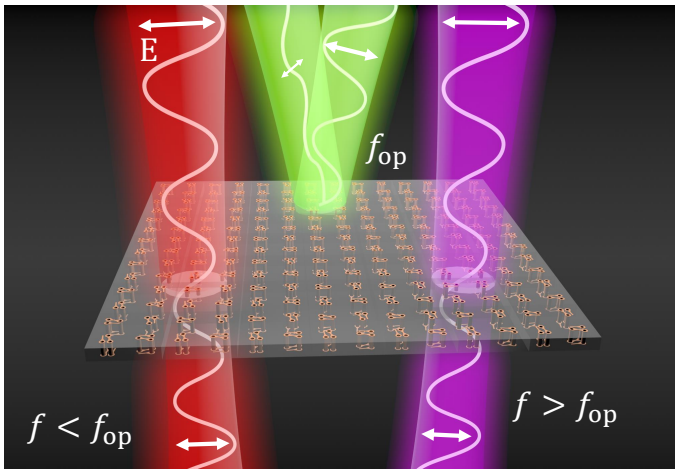

Fig. 1: Conceptual illustration of a metasurface with the desired properties. Different colors represent incident waves of different frequncies. The metasurface fully reflects incident waves into cross-polarization at the operational band $f_{\rm op}$, while completely transmits other frequencies. The white lines depict oscillations of the electric field $\mathbf{E}$.

are properly chosen. First, let us address the first requirement. It can be satisfied only if the reflection coefficient from the metasurface is nearly zero in a wide frequency range, meaning that all the dipole moments induced in the metasurface inclusions scatter destructively in the backward direction. Such scenario can be realized with metasurfaces whose unit cell comprises an orthogonal pair of electric and magnetic dipole moments with the same phases and normalized amplitudes (so-called Huygens' pair). Indeed, the radiation pattern of a combination of two orthogonal electric and magnetic dipole moments has a null in the backward direction, resulting in zero reflection from an array of such unit cells. However, in most previous works, the electric and magnetic moments of the Huygens' pair are formed by two different current modes, either supported by two separate scatterers [19], [20], [22] or excited in a single multi-mode inclusion [17], [18], [25], [33]–[37]. Due to this fact, the dispersions of the electric $\alpha_{\rm ee}$ and magnetic $\alpha_{\rm mm}$ polarizabilities of the unit cell, generally speaking, are different, resulting in different dispersions of the electric $p = \alpha_{\rm ee} E_{\rm loc}$ and magnetic $m = \alpha_{\rm mm} E_{\rm loc}/\eta_0$ dipole moments ($E_{\rm loc}$ is the local electric field and η_0 is the free-space wave impedance). Modelling the polarizabilities using the conventional Lorentz dispersion model, one can write the following relations for the dipolar polarizabilities of the unit cell of an arbitrary geometry:

$$\alpha_{\rm ee} = \frac{A_{\rm e}}{\omega_{\rm e}^2 - \omega^2 + j\omega\gamma_{\rm e}}, \quad \alpha_{\rm mm} = \frac{A_{\rm m}\omega^2}{\omega_{\rm m}^2 - \omega^2 + j\omega\gamma_{\rm m}}, \quad (1)$$

where $\gamma_{\rm e}$ and $\gamma_{\rm m}$ are the loss factors of the electric and magnetic modes of the unit cell, respectively, $A_{\rm e}$ and $A_{\rm m}$ are the amplitude coefficients, $\omega_{\rm e}$ and $\omega_{\rm m}$ are the angular frequencies of the electric and magnetic resonances. Here, time-harmonic dependency in the form $e^{j\omega t}$ is assumed. In order to design a broadband Huygens' metasurface, the dipole moments in each unit cell must be related as $\eta_0 p = m$ in a wide frequency range, meaning that the normalized polarizabilities must be equal $\eta_0\alpha_{\rm ee} = \alpha_{\rm mm}/\eta_0$. As is seen from (1), the electric and magnetic polarizabilities have different frequency dependences due to the ω^2 term in the numerator [38, Eqs. (7.55)–(7.60)]. This fundamental difference is due to the fact that the electric polarization is proportional to the induced electric charge in the inclusion, while the magnetic polarization is proportional to the induced current. It can be understood by considering the limit of the electric and magnetic polarizabilities of an arbitrary non-magnetic passive inclusion at zero frequency, $\omega = 0$. In this case, static electric field creates electric charge separation in the inclusion, resulting in non-zero electric polarizability $\alpha_{\rm ee} = A_{\rm e}/\omega_{\rm e}^2$. On the other hand, polarization currents in the inclusions cannot exist since, according to Faraday's law, it would require alternating magnetic flux through the inclusion (which is zero in statics). Therefore, the induced magnetic dipole moment as well as magnetic polarizability are zero at $\omega = 0$, which is in agreement with (1).

In fact, term ω^2 in the numerator of (1) produces a noticeable deviation only at frequencies far from the resonance where meta-atoms are very weakly excited in any case. Therefore, it is enough to match the other three parameters in (1):

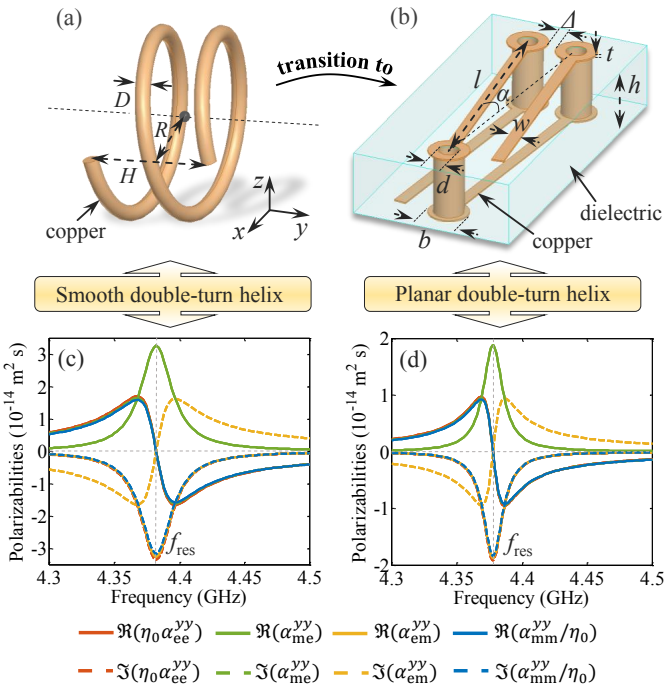

Fig. 2: Single-wire bianisotropic (chiral) inclusions. (a) Smooth double-turn helix with dimensions $D = 0.4$ mm, $R = 2.33$ mm, and $H = 3.23$ mm. (b) Planar double-turn helix with the following parameters: $d = 0.5$ mm, $l = 6.5$ mm, $\Delta = 0.317$ mm, $t = 35$ μm, $h = 1.575$ mm, $w = 0.3$ mm, $b = 1.1$ mm, and $\alpha = 21.6°$. Calculated axial components of the polarizabilities for (c) a smooth and (d) planar bianisotropic inclusion.

Resonance frequencies $\omega_{\rm e,m}$, amplitudes $A_{\rm e,m}$, and loss factors $\gamma_{\rm e,m}$. Nearly perfect matching of the first two parameters can be achieved in a lossless Huygens' pair via precise engineering of the inclusion geometry and their mutual interaction [25]. However, in the general case when absorption is not negligible ($\gamma_{\rm e,m} \neq 0$), simultaneous matching of the loss factors becomes a serious challenge. Since the current distributions of the electric and magnetic modes are different, to ensure equal loss factors $\gamma_{\rm e} = \gamma_{\rm m}$, one must engineer specific *spatial variation* of the material properties (e.g., conductivity) within the unit cell.

The alternative route to satisfy the polarizability balance $\eta_0\alpha_{\rm ee} = \alpha_{\rm mm}/\eta_0$ of the metasurface unit cell in a wide frequency range is based on the use of bianisotropic inclusions constructed by a single metal wire [23], [24], [39]–[42]. In such inclusions, the induced electric and magnetic dipole moments are defined by the same current distribution (mode) along the wire. Therefore, the resonance frequencies $\omega_{\rm e,m}$ and the loss factors $\gamma_{\rm e,m}$ automatically become matched. The only required adjustment is to tune the amplitudes $A_{\rm e} = A_{\rm m}$, which can be done by simple geometry modification. Figure 2a depicts an example of such a single-wire bianisotropic inclusion [23], [39]. The inclusion is a double-turn copper helix with the properly chosen diameter-to-height ratio. Its electric $\alpha_{\rm ee}^{yy}$, magnetic $\alpha_{\rm mm}^{yy}$, and magnetoelectric $\alpha_{\rm em}^{yy}$ (see the basis in Fig. 2a) polarizabilities read [43]

$$\alpha_{\rm ee}^{yy} = \frac{l_{\rm eff}^2}{j\omega}\frac{1}{Z_{\rm inp}},\ \alpha_{\rm mm}^{yy} = -\mu_0^2\frac{j\omega S_{\rm eff}^2}{Z_{\rm inp}},\ \alpha_{\rm em}^{yy} = -\mu_0\frac{S_{\rm eff}l_{\rm eff}}{Z_{\rm inp}}, \tag{2}$$

where $l_{\rm eff}$ and $S_{\rm eff}$ are the length of the effective electric dipole antenna and the area of the effective loop antenna, respectively, $Z_{\rm inp}$ is the frequency dependent input impedance of the helix. The non-zero magnetoelectric polarizability $\alpha_{\rm em}^{yy}$ is due to bianisotropy of the inclusion. From (2) it is seen that the electric and magnetic polarizabilities differ only by the ω^2 multiplier whose influence was discussed above. Therefore, broadband matching of $\alpha_{\rm ee}^{yy}$ and $\alpha_{\rm mm}^{yy}$ can be achieved just by adjusting the effective geometric parameters $l_{\rm eff}$ and $S_{\rm eff}$ which are proportional to the height and the diameter of the helix. Figure 2c plots the frequency dispersion of the polarizabilities of the helix retrieved through the semi-analytical approach [44]. It is seen that all three polarizability components follow nearly the same Lorentzian curve in the resonance frequency range. The deviation between the electric and magnetic polarizabilities at a non-resonance frequency $\omega = m\omega_{\rm res}$ (m is a real multiplier and $\omega_{\rm res}$ is the resonance angular frequency) can be analytically estimated from (1): $\eta_0^2\alpha_{\rm ee}(\omega)/\alpha_{\rm mm}(\omega) = 1/m^2$. For example, at frequencies 4.3 GHz ($\omega \approx 0.982\omega_{\rm res}$) and 4.5 GHz ($\omega \approx 1.027\omega_{\rm res}$), the deviation between the polarizabilities does not exceed 4% and 6%, respectively. It should be noted that the non-axial components of the polarizability tensor of the helix are negligibly small (within the considered frequency band) compared to the axial components in (2), and therefore, are not shown in Fig. 2c.

The main disadvantage of all known single-wire Huygens' inclusions is that they have three-dimensional topology not suitable for simple and commercially available fabrication techniques [23], [24], [39]–[42] (the exception is the direct laser writing technique which can be used for fabricating metasurfaces for the infrared and terahertz frequencies). This fact prevents effective implementation of metasurfaces based on these inclusions. To satisfy our second objective for the design of functional broadband Huygens' metasurfaces, we propose a novel printed-board topology of bianisotropic inclusions shown in Fig. 2b which was inspired by similar meta-atom configuration proposed earlier in Ref. [26]. It implies copper patterning on the two sides of a dielectric spacer with copper vias connecting the two sides. The geometry of the inclusion, resembling that of the smooth double-turn helix, is planar and, therefore, can be easily manufactured with the conventional printed circuit board technology. Adjusting the magnetic polarizability by the effective loop area (h and l) and the electric polarizability by the height of the helix (α and Δ), we can match them in a broad frequency range, as shown in Fig. 2d. The polarizabilities were calculated assuming vacuum spacer. It should be noted that the presence of a dielectric spacer different from vacuum will inevitably create a disbalance between frequency dispersions of the electric and magnetic polarizabilities. However, for low-permittivity spacers, the disbalance will be not pronounced and can be partially (at the resonance band) eliminated by increasing the

magnetic response of the inclusion wire. As it will be shown below (see Section III-A), adding a dielectric substrate with the permittivity $\epsilon_{\rm r} = 2.2$, which we used for the metasurfaces, creates deviation between polarizabilities $\eta_0\alpha_{\rm ee}$ and $\alpha_{\rm mm}/\eta_0$ of 52% at the resonance frequency. In order to compensate this disbalance, we increased the strip length l from 6.5 mm to 7.5 mm to improve the magnetic response. Thus, the unit cell shown in Fig. 2b complies with our both objectives, to be transparent outside the resonance band and have simple topology that can be fabricated with accessible methods.

III. Design of broadband Huygens' metasurfaces for wave control

Let us consider normal plane wave incidence on an infinite periodic metasurface consisting of an array of subwavelength meta-atoms. The periodicity is assumed to be smaller than the wavelength at the metasurface resonance so that no diffraction effects occur for the normal incidence and the surface can be described as a homogeneous current sheet (superposition of electric and magnetic surface current sheets). Moreover, in this work, we assume that the metasurface is reciprocal and only diagonal components of the polarizability dyadics (in the metasurface plane) are non-zero. In this scenario, the electric fields of the reflected and transmitted waves through the metasurface can be expressed in terms of *collective* polarizabilities (marked with hats) of the unit cells [26]:

$$\begin{aligned}\mathbf{E}_{\rm r} = -\frac{j\omega}{2S}\Bigg[&\left(\eta_0\widehat{\alpha}_{\rm ee}^{\rm xx} - \frac{1}{\eta_0}\widehat{\alpha}_{\rm mm}^{\rm yy}\right)\mathbf{xx} + \left(\widehat{\alpha}_{\rm em}^{\rm xx} - \widehat{\alpha}_{\rm em}^{\rm yy}\right)\mathbf{yx} \\ &+ \left(\widehat{\alpha}_{\rm em}^{\rm xx} - \widehat{\alpha}_{\rm em}^{\rm yy}\right)\mathbf{xy} + \left(\eta_0\widehat{\alpha}_{\rm ee}^{\rm yy} - \frac{1}{\eta_0}\widehat{\alpha}_{\rm mm}^{\rm xx}\right)\mathbf{yy}\Bigg]\cdot\mathbf{E}_{\rm inc},\end{aligned} \tag{3}$$

$$\begin{aligned}\mathbf{E}_{\rm t} = \Bigg\{&\left[1 - \frac{j\omega}{2S}\left(\eta_0\widehat{\alpha}_{\rm ee}^{\rm xx} + \frac{1}{\eta_0}\widehat{\alpha}_{\rm mm}^{\rm yy}\right)\right]\mathbf{xx} \\ &+ \frac{j\omega}{2S}\left(\widehat{\alpha}_{\rm em}^{\rm xx} + \widehat{\alpha}_{\rm em}^{\rm yy}\right)\mathbf{yx} \\ &+ \left[1 - \frac{j\omega}{2S}\left(\eta_0\widehat{\alpha}_{\rm ee}^{\rm yy} + \frac{1}{\eta_0}\widehat{\alpha}_{\rm mm}^{\rm xx}\right)\right]\mathbf{yy} \\ &- \frac{j\omega}{2S}\left(\widehat{\alpha}_{\rm em}^{\rm xx} + \widehat{\alpha}_{\rm em}^{\rm yy}\right)\mathbf{xy}\Bigg\}\cdot\mathbf{E}_{\rm inc},\end{aligned} \tag{4}$$

where S is the unit-cell area and $\mathbf{xy}$ denotes the dyadic product of two vectors $\mathbf{x}$ and $\mathbf{y}$. In this basis, the incident wave propagation is assumed towards the $-\mathbf{z}$ direction. The collective polarizabilities take into account the interaction of the unit cells. They can be found as functions of individual polarizabilities as well as electric and magnetic interaction constants. These expressions for the general bianisotropic case can be found in [26, Eqs. (7)–(10)], while for the simple anisotropic case the reader is referred to [45, Eqs. (6)]. Thus, choosing desired reflected and transmission coefficients, one can determine required collective and, subsequently, individual polarizabilities of each unit cell.

A. Absorber

In our previous work [23], we demonstrated that metasurfaces based on smooth helices made of a material with specific conductivity can be designed for complete absorption of incident plane waves at the resonant frequency of the array. Here, we utilize the same concept for synthesizing a planar printed-board-like absorber. To achieve the total absorption of electromagnetic waves, one should ensure that at the operational frequency the reflection and transmission are simultaneously eliminated, that is $\mathbf{E}_{\rm r} = 0$ and $\mathbf{E}_{\rm t} = 0$. This requirement applied to (3) and (4) leads to the following conditions on the collective polarizabilities:

$$\begin{gathered}\eta_0\widehat{\alpha}_{\rm ee}^{\rm xx} = \eta_0\widehat{\alpha}_{\rm ee}^{\rm yy} = \frac{1}{\eta_0}\widehat{\alpha}_{\rm mm}^{\rm xx} = \frac{1}{\eta_0}\widehat{\alpha}_{\rm mm}^{\rm yy} = \frac{S}{j\omega}, \\ \widehat{\alpha}_{\rm em}^{\rm xx} = \widehat{\alpha}_{\rm em}^{\rm yy} = 0.\end{gathered} \tag{5}$$

As is seen, the electric and magnetic responses must be balanced while the chiral magnetoelectric coupling must vanish on the level of the unit cell [46]. Moreover, the collective electric and magnetic polarizabilities must be purely imaginary, meaning that full absorption can occur only at the resonance of the grid. From (5) it is also can be deduced that the obtained values for the collective polarizabilities correspond to those of lossy inclusions. Indeed, if the inclusions are lossless, the imaginary parts of their collective polarizabilities would obey equalities $\Im(1/\widehat{\alpha}_{\rm ee}) = \eta_0\omega/(2S)$ and $\Im(1/\widehat{\alpha}_{\rm mm}) = \omega/(2S\eta_0)$ [47, Eqs. (4.87)], which contradicts to Eqs. (5).

Following the idea proposed in [23], [39], we place several chiral helices of opposite handedness in each unit cell (see Fig. 3a) so that the magnetoelectric coupling is compensated, i.e. $\widehat{\alpha}_{\rm em}^{\rm xx} = \widehat{\alpha}_{\rm em}^{\rm yy} = 0$. Note that the use of bianisotropic inclusions is necessary since we aim at realizing a broadband transparent metasurface (see the discussion in Section II). The proper dimensions of the planar helices were chosen based on requirements (5) using the polarization extraction approach [44] and final numerical optimization of the metasurface. All the dimensions are listed in the caption of Fig. 3.

The metasurface was fabricated with conventional printed circuit board technology by etching copper cladding on both sides of a dielectric substrate (we used Rogers 5880 for all metasurfaces; $\epsilon_{\rm r} = 2.2$, $\tan\delta = 0.0009$) and connecting the patterns in the proper positions by metallized vias. Figure 3b depicts the fabricated metasurface sample of 360×260 mm^2 size ($\approx 3.91\lambda_{\rm res} \times 2.82\lambda_{\rm res}$, where $\lambda_{\rm res}$ is the resonance wavelength) consisting of 6×4 unit cells.

Based on the full-wave simulations [48], we calculated the reflection, transmission, and absorption coefficients for an *infinite* absorbing metasurface (see Fig. 3c). At the operational frequency of 3.24 GHz, the metasurface absorbs 96.9% of the incident power. At the same time, it remains transparent ($|T|^2 \geq 80\%$) from 0 Hz to 3.22 GHz and from 3.28 GHz to 6.67 GHz. At higher frequencies, some reflection peaks appear due to excitation of higher order current modes in the helices [23], [25]). Also it is seen from Fig. 3c that at high frequencies the reflectance becomes noticeable (around 5.5% at 6 GHz) due to the permittivity contrast between the dielectric substrate and air.

Next, we performed experimental verification of the metasurface functionality. Due to relatively small size of the printed sample (each side is just a few wavelengths long), it was expected that the scattering at the edges of the metasurface

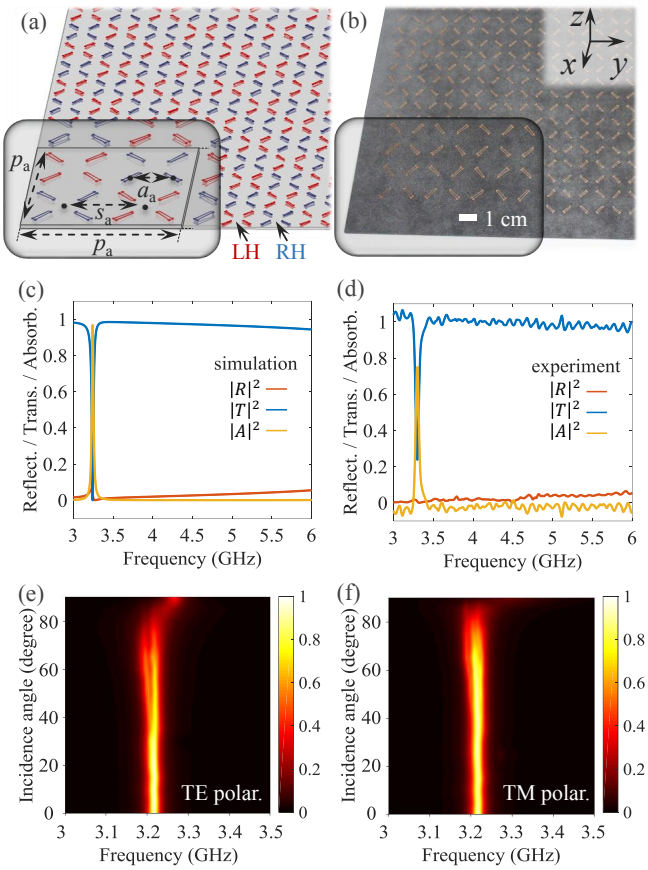

Fig. 3: (a) Schematic image of the absorbing metasurface with structural parameters: $s_\mathrm{a} = 28$ mm ($\approx 0.3\lambda_\mathrm{res}$), $p_\mathrm{a} = 2s_\mathrm{a}$ ($\approx 0.6\lambda_\mathrm{res}$), and $a_\mathrm{a} = 14$ mm ($\approx 0.15\lambda_\mathrm{res}$). Right- and left-handed planar helices are shown in blue and red, respectively. The planar helix in this design has the following specifications: $d = 0.5$ mm, $l = 7.5$ mm, $\Delta = 0.317$ mm, $t = 35$ μm, $h = 1.575$ mm, $w = 0.3$ mm, $b = 1.1$ mm, and $\alpha = 21.6°$. (b) Photograph of the absorbing metasurface fabricated using the printed circuit board technique. (c) Simulated reflectance ($|R|^2$), transmittance ($|T|^2$), and absorbance ($|A|^2$) from the infinite metasurface. (d) Corresponding coefficients extracted from measurements of the finite-size metasurface. Simulated absorbance as a function of the incidence angle for (e) TE and (f) TM polarizations, respectively.

will be significant and conventional measurement approaches (assuming that the incident wave beam is smaller in width than the sample size) will not provide accurate results. Therefore, we exploited the alternative technique based on the physical optics approximation [49, ch. 8]. Its main assumption is that the effective polarization currents flowing in the metasurface at each point are determined by the value of the incident field only at this very point. First, these effective currents are determined over the sample aperture, knowing the incident field and the local reflection coefficient. The latter one, according to the aforementioned assumption, is taken identical for points at the center and at the edges of the sample (if the sample is uniform). Second, the magnetic vector potential and scattered fields are calculated for the known distribution of the effective currents. Therefore, this approach approximately (in the physical optics approximation) takes into account scattering from the edges and allows one to determine the reflection and transmission coefficients from a metasurface sample of a finite size. The reader is referred to Section IV for more details about this approach. Figure 3d shows the frequency dispersion of the reflection, transmission, and absorption coefficients extracted from the measured data. The experimental results are in good agreement with the simulated ones and confirm transparency of the absorbing metasurface at non-resonant frequencies. The absorption peak in the experiment reaches only 75%, which we explain by possible imperfections of the time gating window used in the measurements to filter parasitic signals. At frequencies below the resonance, the electrical size of the metasurface becomes even smaller and the assumption of the current uniformity does not hold any more, resulting in non-physical transmittance slightly higher than unity.

Figures 3e and 3f demonstrate simulated angular response of the absorbing metasurface. It is seen that for both TE and TM polarizations, the metasurface effectively absorbs incident plane waves at oblique angles up to 65°. At frequencies outside the resonance band and for arbitrary incident angles, absorption is negligible.

B. Twist polarizer in transmission

Polarization rotation of electromagnetic waves in transmission was for the first time observed by Arago in 1811. Conventional structures with this functionality are various cascades of wire-grid polarizers whose wires are oriented in different directions in different layers (see e.g. [50], [51]) and optically anisotropic planar arrays of meta-atoms [52], [53]. However, all of these structures operate only with one polarization of incident waves. To achieve uniaxial polarization rotation, the material slab or metasurface must have non-zero chiral properties, i.e. $\widehat{\alpha}_\mathrm{em} \neq 0$ (e.g., [54]). Currently, there has been proposed a great variety of different chiral metasurfaces operating as twist polarizers (for arbitrary polarization) in transmission [26], [55]–[58]. However, only one of them simultaneously combined properties of off-band transparency and planar topology suitable for easy fabrication [26]. The drawback of that design is the low efficiency of cross-polarized transmission (about 45%). The deficiency occurred due to imbalanced electric and magnetic responses of the unit cell and could not be eliminated without significant modifications of the unit-cell geometry. The topology of the unit cell that is utilized in this work (see Fig. 2b) allows one to overcome this problem.

The requirements of uniaxial polarization rotation in transmission are zero reflection $\mathbf{E}_\mathrm{r} = 0$ and unity-amplitude transmitted field in cross polarization with arbitrary additional phase ϕ, i.e. $\mathbf{E}_\mathrm{t} = e^{j\phi}\mathbf{n} \times \mathbf{E}_\mathrm{i}$, where $\mathbf{n}$ is a normal unit vector pointing towards the direction opposite to the incident wave propagation. Such formulation ensures that an arbitrary linear polarization of incident waves is always rotated by angle

90° in the anti clockwise direction (if $\phi = 0°$). Applying the requirements of uniaxial polarization rotation to (3) and (4), one obtains the following conditions on the collective polarizabilities:

$$\eta_0\widehat{\alpha}_{\rm ee}^{\rm xx} = \eta_0\widehat{\alpha}_{\rm ee}^{\rm yy} = \frac{1}{\eta_0}\widehat{\alpha}_{\rm mm}^{\rm xx} = \frac{1}{\eta_0}\widehat{\alpha}_{\rm mm}^{\rm yy} = \frac{S}{j\omega},$$
$$\widehat{\alpha}_{\rm em}^{\rm xx} + \widehat{\alpha}_{\rm em}^{\rm yy} = -e^{j\phi}\frac{2S}{j\omega}. \qquad (6)$$

As is seen, the electric and magnetic responses must be balanced as in a Huygens' unit cell, while chirality must not be compensated as in the previous example. Therefore, we design a unit cell consisting of four right-handed planar helices as shown in Fig. 4a. In this case, the phase of cross-polarized transmission is $\phi = 90°$ and $\widehat{\alpha}_{\rm em}^{\rm xx} = \widehat{\alpha}_{\rm em}^{\rm yy} = -S/\omega$ [26]. The parameters of the inclusions were modified to demonstrate that the metasurfaces based on them can be designed for an arbitrary frequency (within a reasonably wide frequency range). It should be noted that the change of the frequency requires modification of the geometry of the inclusions and in some cases may require the use of a substrate with a different thickness (see the structural parameters in the figure caption). The fabricated sample, shown in Fig. 4b, was of 260×180 mm^2 size ($\approx 3.77\lambda_{\rm res} \times 2.61\lambda_{\rm res}$) and included 16×11 unit cells. Figures 4c and d show the simulated co- and cross-polarized reflectance and transmittance extracted from the simulated infinite-size and measured finite-size metasurfaces, respectively. The metasurface is transparent ($|T_{\rm co}|^2 \geq 80\%$) from 0 Hz to 4.1 GHz and from 4.52 GHz to 7.15 GHz. At the resonance frequency, the simulated cross-polarized transmittance is smaller than unity due to absorption in the dielectric substrate and small parasitic reflections. The measured peak of cross-polarized transmittance reaches only 50%, which we explain by the relatively small electrical size of the sample, compromising the physical optics approximation (which assumes currents at the metasurface and at the reference metal plate be uniform everywhere, including edges), and possible time gating inaccuracies. Moreover, to find the cross polarized transmittance, we normalized the *cross*-polarized signal transmitted through the metasurface by the *co*-polarized signal transmitted through a reference metal plate. Thus, the signals transmitted through the metasurface and the metal plate were received by different ports of the antenna, experiencing different absorption levels in the measurement setup. This fact does not allow us to accurately calculate the cross-polarized transmission. Importantly, the resonance frequencies as well as off-band transparency properties are in agreement in both simulations and measurements.

The efficiency of polarization rotation can be also characterized by the polarization rotation angle θ and ellipticity ψ of the transmitted waves. These parameters can be expressed as follows [59]:

$$\theta = \frac{1}{2}\left[\arg(T_{\rm RCP}) - \arg(T_{\rm LCP})\right] \qquad (7)$$

$$\psi = \frac{1}{2}\arcsin\left(\frac{|T_{\rm RCP}|^2 - |T_{\rm LCP}|^2}{|T_{\rm RCP}|^2 + |T_{\rm LCP}|^2}\right), \qquad (8)$$

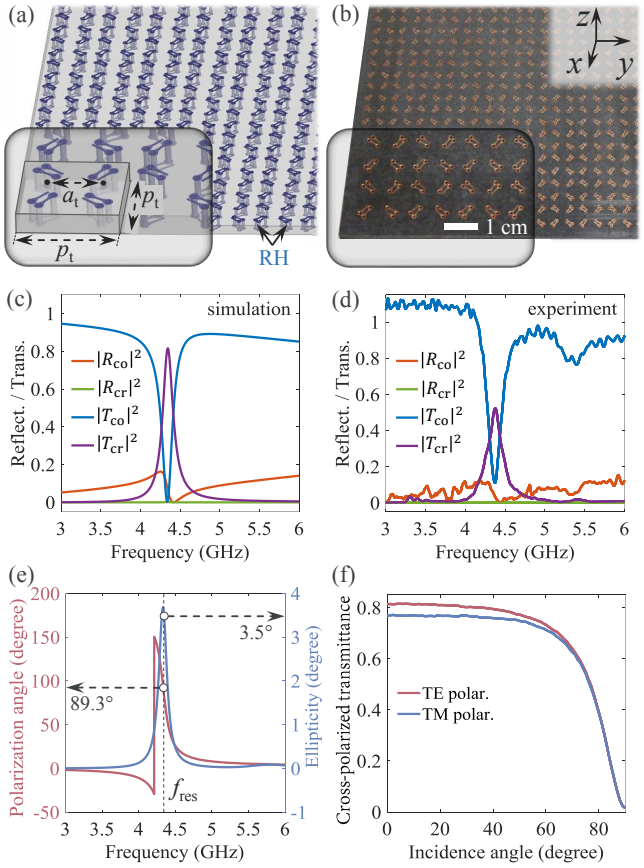

Fig. 4: (a) Schematic image of the twist transmitter with structural parameters: $p_{\rm t} = 15.6$ mm ($\approx 0.23\lambda_{\rm res}$) and $a_{\rm t} = 7.8$ mm ($\approx 0.11\lambda_{\rm res}$). The planar helix in this design has the following specifications: $d = 0.8$ mm, $l = 3.5$ mm, $\Delta = 0.226$ mm, $t = 70$ μm, $h = 3.175$ mm, $w = 0.3$ mm, $b = 1.4$ mm, and $\alpha = 27°$. (b) Photograph of the twist transmitter sample. (c) Simulated co- and cross-polarized reflectance ($|R_{\rm co}|^2$ and $|R_{\rm cr}|^2$) and transmittance ($|T_{\rm co}|^2$ and $|T_{\rm cr}|^2$) from the infinite metasurface. (d) Corresponding coefficients extracted from measurements of the finite-size metasurface. (e) Polarization rotation angle θ and ellipticity ψ of transmitted waves through the metasurface at the normal incidence. (f) Cross-polarized transmittance at the resonance frequency for TE and TM polarizations.

where $T_{\rm RCP} = T_{\rm co} + jT_{\rm cr}$ and $T_{\rm LCP} = T_{\rm co} - jT_{\rm cr}$ are the transmission coefficients of the right- and left-circular polarized waves, respectively. The polarization rotation angle θ represents the angle between the polarization planes of the incident and transmitted waves, while the ellipticity ψ measures the polarization state of the transmitted wave. Pure transformation to the cross-polarized transmitted wave corresponds to the case when the ellipticity is equal to zero ($\psi = 0°$) while the polarization plane has rotation angle of $\theta = 90°$ with respect to the normal incidence. Figure 4e shows the simulated polarization rotation angle and ellipticity of transmitted waves through the designed twist transmitter.

As is seen, the polarization angle and ellipticity are equal to $\theta = 89.3°$ and $\psi = 3.5°$ at the resonance frequency of $f_{\rm res} = 4.33$ GHz. This result confirms the high polarization purity of the designed twist polarizer. Figure 4f shows simulated cross-polarized transmittance of the metasurface as a function of the incidence angle for TE and TM linearly polarized waves. One can see that high level of the cross-polarized transmittance $|T_{\rm cr}|^2 > 60\%$ is retained for up to 70° for both polarizations.

C. Polarization rotator in reflection

Another device that can be build based on the broadband Huygens' cell shown in Fig. 2b is a reflector which rotates polarization of the incident wave by 90°. Due to reciprocity, the rotation directions are opposite for vertical and for horizontal linear polarizations of incident waves. Conventional structures rotating polarization of reflected waves are anisotropic metasurfaces backed with a ground plane [60]–[62]. Obviously, these devices block incident waves of all frequencies.

By requiring zero transmission through the metasurface $\mathbf{E}_{\rm t} = 0$ and unitary cross-polarized reflection $\mathbf{E}_{\rm r} = -e^{j\phi}(\mathbf{xy} + \mathbf{yx}) \cdot \mathbf{E}_{\rm i}$, from (3) and (4), one can derive the following conditions on the collective polarizabilities:

$$\eta_0\widehat{\alpha}_{\rm ee}^{\rm xx} = \eta_0\widehat{\alpha}_{\rm ee}^{\rm yy} = \frac{1}{\eta_0}\widehat{\alpha}_{\rm mm}^{\rm xx} = \frac{1}{\eta_0}\widehat{\alpha}_{\rm mm}^{\rm yy} = \frac{S}{j\omega},$$
$$\widehat{\alpha}_{\rm em}^{\rm xx} - \widehat{\alpha}_{\rm em}^{\rm yy} = e^{j\phi}\frac{2S}{j\omega}. \qquad (9)$$

Interestingly, these requirements are very similar to (6) with the only difference in one sign in the last equation. However, the realization of the polarization rotator in reflection differs from that of the twist polarizer for transmitted waves. According to the last equation in (9), the unit cell cannot be isotropic in the plane that would imply $\widehat{\alpha}_{\rm em}^{\rm xx} = \widehat{\alpha}_{\rm em}^{\rm yy}$. As a canonical solution, we propose to arrange in one unit cell left- and right-handed inclusions along the x and y axes, respectively, so that $\widehat{\alpha}_{\rm em}^{\rm xx} = -\widehat{\alpha}_{\rm em}^{\rm yy} = S/\omega$. The geometry of the unit cell can be seen in Fig. 5a. The fabricated sample was of 260×180 mm size ($\approx 4.44\lambda_{\rm res} \times 3.08\lambda_{\rm res}$) and included 16×11 unit cells (shown in Fig. 5b). Both simulated (Fig. 5c) and measured (Fig. 5d) data reveal the resonance frequency of 5.13 GHz. The metasurface remains transparent ($|T|^2 \geq 80\%$) from 0 Hz to 4.83 GHz and from 5.28 GHz to 8.45 GHz. The simulated peak of the cross reflectance is at 75% due to relatively high absorption loss (about 14%) and parasitic co-polarized reflections (about 11%). The measured peak reaches 30%. Such low value could be due to several factors: The inaccuracies of the physical optics approximation technique applied to the data processing for the sample with a relatively small electrical size, non-ideal time gating window, and non-ideal plane-wave illumination, etc. At frequencies below the resonance, the electrical size of the metasurface becomes smaller and the assumption of the current uniformity becomes less adequate, resulting in non-physical transmittance higher than unity. Nevertheless, both simulated and experimental data confirm that the metasurface is highly transparent at frequencies outside the resonance.

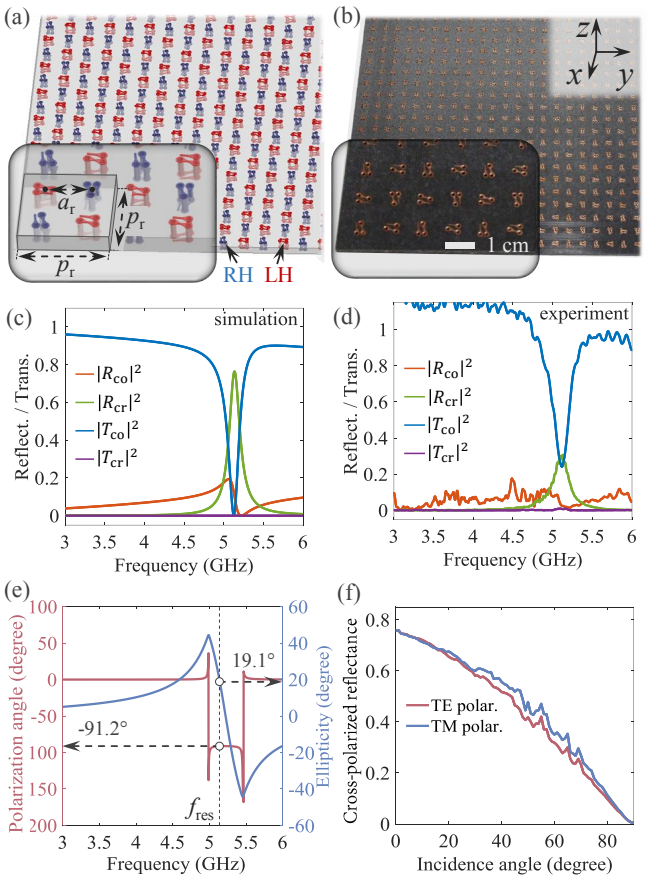

Fig. 5: (a) Schematic image of the metasurface rotating polarization in reflection with structural parameters: $p_{\rm r} = 16$ mm ($\approx 0.27\lambda_{\rm res}$) and $a_{\rm r} = 8$ mm ($\approx 0.14\lambda_{\rm res}$). The planar helix in this design has the following specifications: $d = 0.8$ mm, $l = 2.8$ mm, $\Delta = 0.24$ mm, $t = 70$ μm, $h = 3.175$ mm, $w = 0.3$ mm, $b = 1.4$ mm, and $\alpha = 34°$. (b) Photograph of the fabricated sample. (c) Simulated co- and cross-polarized reflectance and transmittance from the infinite metasurface. (d) Corresponding coefficients extracted from measurements of the finite-size metasurface. (e) Polarization rotation angle and ellipticity of reflected waves from the metasurface at the normal incidence. (f) Cross-polarized reflectance at the resonance frequency for TE and TM polarizations.

It should be noted that the proposed polarization rotator in reflection behaves as the so-called "chiral mirror" [63]. In contrast to conventional mirrors (perfect electric or magnetic conductors), the metasurface totally reflects circularly polarized incident waves preserving their handedness. In order to verify this property of the proposed structure, we derive from (3) and (4) the following relations for reflection and transmission coefficients in the basis of circularly polarized

waves:

$$R_{\mathrm{RR/LL}} = \frac{j\omega}{4S}(\eta_0\widehat{\alpha}_{\mathrm{ee}}^{\mathrm{yy}} - \eta_0\widehat{\alpha}_{\mathrm{ee}}^{\mathrm{xx}} - \frac{1}{\eta_0}\widehat{\alpha}_{\mathrm{mm}}^{\mathrm{xx}} + \frac{1}{\eta_0}\widehat{\alpha}_{\mathrm{mm}}^{\mathrm{yy}} \mp 2j\widehat{\alpha}_{\mathrm{em}}^{\mathrm{xx}} \pm 2j\widehat{\alpha}_{\mathrm{em}}^{\mathrm{yy}}),$$

$$R_{\mathrm{RL}} = R_{\mathrm{LR}} = -\frac{j\omega}{4S}(\eta_0\widehat{\alpha}_{\mathrm{ee}}^{\mathrm{xx}} + \eta_0\widehat{\alpha}_{\mathrm{ee}}^{\mathrm{yy}} - \frac{1}{\eta_0}\widehat{\alpha}_{\mathrm{mm}}^{\mathrm{xx}} - \frac{1}{\eta_0}\widehat{\alpha}_{\mathrm{mm}}^{\mathrm{yy}}),$$

$$T_{\mathrm{RR/LL}} = 1 - \frac{j\omega}{4S}(\eta_0\widehat{\alpha}_{\mathrm{ee}}^{\mathrm{xx}} + \eta_0\widehat{\alpha}_{\mathrm{ee}}^{\mathrm{yy}} + \frac{1}{\eta_0}\widehat{\alpha}_{\mathrm{mm}}^{\mathrm{xx}} + \frac{1}{\eta_0}\widehat{\alpha}_{\mathrm{mm}}^{\mathrm{yy}} \pm 2j\widehat{\alpha}_{\mathrm{em}}^{\mathrm{xx}} \pm 2j\widehat{\alpha}_{\mathrm{em}}^{\mathrm{yy}}),$$

$$T_{\mathrm{RL/LR}} = \frac{j\omega}{4S}(\eta_0\widehat{\alpha}_{\mathrm{ee}}^{\mathrm{yy}} - \eta_0\widehat{\alpha}_{\mathrm{ee}}^{\mathrm{xx}} + \frac{1}{\eta_0}\widehat{\alpha}_{\mathrm{mm}}^{\mathrm{xx}} - \frac{1}{\eta_0}\widehat{\alpha}_{\mathrm{mm}}^{\mathrm{yy}}). \quad (10)$$

Here indices "R" and "L" define, respectively, RCP and LCP polarizations. The double indices in the left-hand sides of the relations correspond to the double signs in the right-hand sides. Now, it is easy to show that the proposed chiral polarization rotator, with polarizabilities given by (9) and $\widehat{\alpha}_{\mathrm{em}}^{\mathrm{xx}} = -\widehat{\alpha}_{\mathrm{em}}^{\mathrm{yy}} = S/\omega$, in fact reflects circularly polarized waves preserving their handedness, i.e. $R_{\mathrm{RR/LL}} = \pm 1$ and $T_{\mathrm{RR/LL}} = T_{\mathrm{RL/LR}} = R_{\mathrm{RL/LR}} = 0$.

The simulated polarization rotation angle and ellipticity of waves reflected from the designed metasurface are plotted in Fig. 5e. Due to the non-zero parasitic co-polarized reflection mentioned above, the ellipticity equals to $= 19.1°$ at the resonance. The polarization angle is $= -91.2°$. Finally, Fig. 5f shows the simulated cross-polarized reflectance of the metasurface as a function of the incidence angle for TE and TM linearly polarized waves. It is seen that in contrast to the two previous metasurfaces, the polarization rotator in reflection possesses higher sensitivity to the incident angle. It can be explained by the fact that the unit cell of the reflecting metasurface is not isotropic in the array plane.

IV. On Experimental Characterization of Finite-Size Samples

Due to the limited size of the fabricated metasurface samples, it was expected that the direct measurements of the reflection and transmission coefficients based on conventional techniques would be very inaccurate. Therefore, instead we exploited the method based on the physical optics approximation [49, ch. 8] which approximately takes into account diffraction on the sample edges. This method is particularly suitable when the sample is so small that incident waves illuminate its whole surface.

A. Co- and cross-polarized reflected fields from a finite-size sample

In this section, we calculate diffraction of a plane wave on a finite-size two-dimensional sample (aperture) with given reflective properties (locally defined reflection coefficients). The calculated scattered field will be subsequently used for normalization of the measured data.

We assume that the metasurface sample is located in the xy-plane and it is illuminated along the $-z$-axis by a plane wave

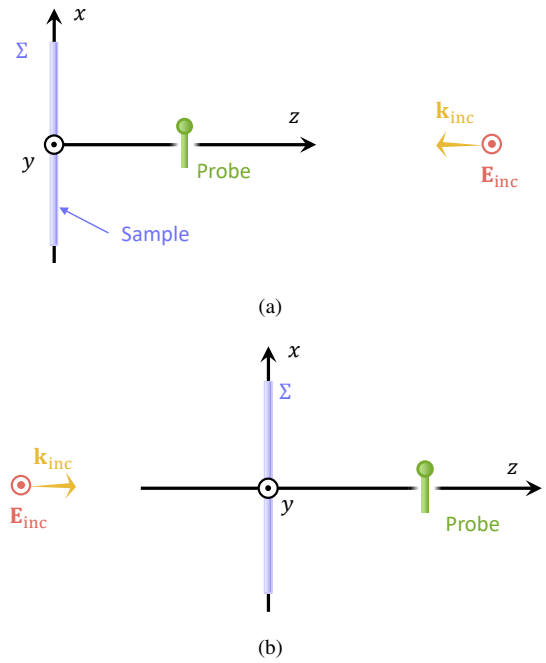

Fig. 6: On measurements of local (a) reflection and (b) transmission coefficients through a metasurface sample of a finite size. The sample is illuminated by a plane wave. The scattered field is measured at distance z.

with electric field $\mathbf{E}_{\mathrm{inc}} = E_0 e^{jk_0 z}\mathbf{y}_0$ (k_0 is the wavenumber of free space), as it is shown in Fig. 6a. The reflected field at each point of the metasurface is defined as

$$\mathbf{E}_{\mathrm{r}} = \bar{\bar{R}}_{\mathrm{s}}(f) \cdot \mathbf{E}_{\mathrm{inc}}(z = 0), \quad (11)$$

where $\bar{\bar{R}}_{\mathrm{s}}$ is the *local* reflection coefficient of the metasurface written in dyadic form using unitary dyadic $\bar{\bar{I}}$ as

$$\bar{\bar{R}}_{\mathrm{s}}(f) = R_{\mathrm{co}}(f)\bar{\bar{I}} + R_{\mathrm{cr}}(f)\mathbf{z}_0 \times \bar{\bar{I}}. \quad (12)$$

Next, one can find the equivalent electric surface current density on the metasurface which creates the given reflected field $\mathbf{E}_{\mathrm{r}} = -\eta_0/2\mathbf{J}_{\mathrm{s}}$. Using (11), this current is given by

$$\mathbf{J}_{\mathrm{s}} = -\frac{2}{\eta_0}\bar{\bar{R}}_{\mathrm{s}}(f) \cdot \mathbf{E}_{\mathrm{inc}}(z = 0). \quad (13)$$

The scattered fields created by the finite-size metasurface with surface current density (13) can be obtained using the magnetic potential vector definition with the Green function:

$$\mathbf{A} = \int_{\Sigma} \mathbf{J}_{\mathrm{s}}(r')G(\mathbf{r} - \mathbf{r}')d^2r', \quad (14)$$

where Σ is the metasurface area. The Green function is defined by the distance between the observation point $\mathbf{r}$, measured from the coordinates' origin, and an arbitrary point of the sample surface $\mathbf{r}'$. If the observation point is defined at a distance z collinear with the incident wave and the arbitrary point at the sample surface is $\mathbf{r}' = x'\mathbf{x}_0 + y'\mathbf{y}_0$, the Green function reads:

$$G(\mathbf{r} - \mathbf{r}') = \frac{e^{-jk_0|\mathbf{r}-\mathbf{r}'|}}{4\pi|\mathbf{r} - \mathbf{r}'|}, \quad (15)$$

$$\mathbf{r} - \mathbf{r}' = z\mathbf{z}_0 + x'\mathbf{x}_0 + y'\mathbf{y}_0. \quad (16)$$

Hence, the back-scattered electric field can be obtained from the magnetic potential vector in (14) and using (15) and (16):

$$\mathbf{E}_{\text{bsc}} = -j\omega\mu_0\mathbf{A} = \frac{jk_0}{2\pi}\bar{\bar{R}}_{\text{s}}(f)\cdot\mathbf{E}_{\text{inc}}(z=0)G_{\text{eff}}(z), \quad (17)$$

where G_{eff} is the "effective Green factor" of the illuminated surface:

$$G_{\text{eff}}(z) = \int_{\Sigma}\frac{e^{-jk_0\sqrt{z^2+x'^2+y'^2}}}{\sqrt{z^2+x'^2+y'^2}}dx'dy'. \quad (18)$$

Using equation (17), it is possible to relate the local co- and cross-polarized reflection coefficients with the back-scattered field at a distance z:

$$\mathbf{E}_{\text{bsc,co}}(z) = \mathbf{y}_0\frac{jk_0}{2\pi}R_{\text{co}}E_0G_{\text{eff}}(z), \quad (19)$$

$$\mathbf{E}_{\text{bsc,cr}}(z) = \mathbf{y}_0\frac{jk_0}{2\pi}R_{\text{cr}}E_0G_{\text{eff}}(z). \quad (20)$$

B. Co- and cross-polarized transmitted fields from a finite-size sample

Next, we calculate scattered fields in the forward direction from a finite-size sample with given transmission properties, that is, the local transmission coefficient. In this scenario, the incident plane wave propagates along the $+z$-axis, and its electric field reads $\mathbf{E}_{\text{inc}} = E_0e^{-jk_0z}\mathbf{y}_0$, as shown in Fig. 6b. The transmitted field at each point of the metasurface is defined as

$$\mathbf{E}_{\text{t}} = \bar{\bar{T}}_{\text{s}}(f)\cdot\mathbf{E}_{\text{inc}}(z=0), \quad (21)$$

where $\bar{\bar{T}}_{\text{s}}$ is the *local* transmission coefficient of the metasurface written in dyadic form as

$$\bar{\bar{T}}_{\text{s}}(f) = T_{\text{co}}(f)\bar{\bar{I}} - T_{\text{cr}}(f)\mathbf{z}_0\times\bar{\bar{I}}. \quad (22)$$

Next, in order to find equivalent electric surface current density $\mathbf{J}_{\text{s}}$ induced on the metasurface, we find the electric field that it scatters locally: $-\eta_0/2\mathbf{J}_{\text{s}} = \mathbf{E}_{\text{sc}} = \mathbf{E}_{\text{t}} - \mathbf{E}_{\text{inc}}$. Therefore, the current density reads

$$\mathbf{J}_{\text{s}} = \frac{2}{\eta_0}\left([1-T_{\text{co}}(f)]\bar{\bar{I}} + T_{\text{cr}}(f)\mathbf{z}_0\times\bar{\bar{I}}\right)\mathbf{E}_{\text{inc}}(z=0). \quad (23)$$

By reusing the result obtained in equations (14)–(17), it is possible to relate the local co- and cross-polarized transmitted coefficients with the forward-scattered field at a distance z:

$$\mathbf{E}_{\text{fsc,co}}(z) = \mathbf{y}_0\frac{jk_0}{2\pi}(T_{\text{co}}-1)E_0G_{\text{eff}}(z), \quad (24)$$

$$\mathbf{E}_{\text{fsc,cr}}(z) = -\mathbf{y}_0\frac{jk_0}{2\pi}T_{\text{cr}}E_0G_{\text{eff}}(z). \quad (25)$$

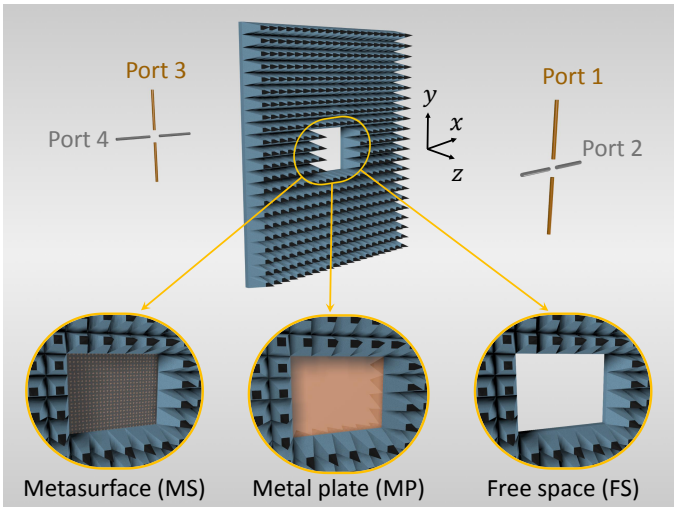

Fig. 7: Illustration of the experimental setup. The fields were measured in two polarizations, vertical (ports 1 and 3) and horizontal (ports 2 and 4). To eliminate all parasitic effects, there were three measurements performed: With a metasurface (MS), with a metal plate (MP), and empty aperture (FS).

C. Extraction of local reflection and transmission coefficients

As it is seen from (19), (20), (24), and (25), in order to find the local reflection/transmission coefficients, one must know the corresponding scattered field at one particular point on the z-axis and the incident field E_0 (also its phase) at the position of the sample. Direct measurement of these fields is not a trivial task. Therefore, in addition to measurements of the metasurface sample, we performed two additional reference measurements: A free-space scenario (the sample was removed) and a reference metal plate (the sample was replaced by a metal plate of the same shape and size). Using the data obtained from these three measurements, we could eliminate all parasitic effects such as losses in the cables, reflections from the walls of the anechoic chamber, mismatch of the antennas, etc. Additionally, time gating was exploited to improve the signal-to-noise ratio.

The experimental setups for all three measurements are illustrated in Fig. 7. A wall made of wideband microwave absorbers was positioned in the sample plane (xy-plane) with an open aperture of the same size. Two identical horn antennas operating with both orthogonal polarizations were located at a distance of approximately 2.5 m (more than 25 times larger than the longest operational wavelength of the metasurfaces) away from the sample. The antennas had dual function, that is to emulate the source of an incident plane wave and to measure the fields at their locations. The terminals of the antennas for measuring vertical and horizontal polarizations were connected to four ports of a vector network analyser (see numeration in Fig. 7). Now, based on the S-parameters measured by the vector network analyser, one can write the following relations for extracting the unknown reflection and transmission coefficients:

$$R_{\rm co} = \frac{S_{11,\rm MS} - S_{11,\rm FS}}{S_{11,\rm MP} - S_{11,\rm FS}} \cdot \frac{G_{\rm eff,MP}}{G_{\rm eff,MS}}, \quad (26)$$

$$R_{\rm cr} = \frac{S_{21,\rm MS} - S_{21,\rm FS}}{S_{11,\rm MP} - S_{11,\rm FS}} \cdot \frac{G_{\rm eff,MP}}{G_{\rm eff,MS}}, \quad (27)$$

$$T_{\rm co} = 1 - \frac{S_{13,\rm MS} - S_{13,\rm FS}}{S_{13,\rm MP} - S_{13,\rm FS}} \cdot \frac{G_{\rm eff,MP}}{G_{\rm eff,MS}}, \quad (28)$$

$$T_{\rm cr} = \frac{S_{23,\rm MS} - S_{23,\rm FS}}{S_{13,\rm MP} - S_{13,\rm FS}} \cdot \frac{G_{\rm eff,MP}}{G_{\rm eff,MS}}. \quad (29)$$

Here, subscripts "MS", "MP", and "FS" correspond to the scenarios shown in Fig. 7 when the aperture in the absorbing wall was filled with a metasurface, metal plate, and left empty (free space), respectively. The effective Green factors appear in (26)–(29) to take into account possible difference in the sizes of the metasurface and the reference metal plate.

The reflectance and transmittance plotted in Fig. 3d were calculated as $|R|^2 = |R_{\rm co}|^2 + |R_{\rm cr}|^2$ and $|T|^2 = |T_{\rm co}|^2 + |T_{\rm cr}|^2$, respectively. The absorption coefficient was calculated as $|A| = 1 - |R|^2 - |T|^2$.

V. Conclusions

In this work, we have proposed a new planar Huygens' meta-atom that possesses balanced electric and magnetic responses in addition to chiral coupling. Importantly, the meta-atom remains highly transparent outside the resonance due to the identical frequency dispersions of its polarizabilities. Metasurfaces based on these Huygens' unit cells can be readily fabricated with conventional printed circuit board technique. This technology is widely used for manufacturing of electronic products and its components in the printed form.

We fabricated three different metasurfaces capable of specific amplitude and polarization transformations. Their potential applications include transparent lenses, passive antenna arrays, and holograms. One can extend the use of Huygens' meta-atoms to the design of gradient PCB-compatible metasurfaces for general wave front manipulations (e.g., focusing and beam deflection with additional polarization transformation). Indeed, as is seen in the captions of Figs. 4 and 5, the unit cell size does not exceed $0.27\lambda_{\rm res}$, resulting in the possibility to fit several of such unit cells in a super-cell of a wavelength-scale size [24]. The design of gradient PCB-compatible metasurfaces can be performed using the traditional approach based on locally-uniform surface approximation [64]. In this case, Eqs. (3) and (4) should be used for synthesizing each unit cell (expressions between the collective and individual polarizabilities will not change). Alternatively, gradient metasurfaces can be designed based on a recently proposed non-local approach which demonstrated significantly higher efficiencies [65]–[69]. Although the Huygens' unit cells proposed in this paper can be still utilized in this case, the theoretical analysis will need to be modified.

Acknowledgement

This work was supported by the Academy of Finland (project 287894) and Nokia Foundation (201610246).

References

[1] J. Huang, "Microstrip reflectarray," in *Antennas and Propagation Society Symposium 1991 Digest*, pp. 612–615 vol.2, June 1991.

[2] D. M. Pozar and T. A. Metzler, "Analysis of a reflectarray antenna using microstrip patches of variable size," *Electronics Letters*, vol. 29, pp. 657–658, Apr. 1993.

[3] D. M. Pozar, S. D. Targonski, and H. D. Syrigos, "Design of millimeter wave microstrip reflectarrays," *IEEE Transactions on Antennas and Propagation*, vol. 45, pp. 287–296, Feb. 1997.

[4] J. Huang and R. J. Pogorzelski, "A Ka-band microstrip reflectarray with elements having variable rotation angles," *IEEE Transactions on Antennas and Propagation*, vol. 46, pp. 650–656, May 1998.

[5] M. R. Chaharmir, J. Shaker, M. Cuhaci, and A. Sebak, "Reflectarray with variable slots on ground plane," *Antennas and Propagation IEE Proceedings - Microwaves*, vol. 150, pp. 436–439, Dec. 2003.

[6] J. Huang and J. A. Encinar, *Reflectarray Antennas*. Piscataway: IEEE Press, 2008.

[7] Z. Popovic and A. Mortazawi, "Quasi-optical transmit/receive front ends," *IEEE Transactions on microwave Theory and Techniques*, vol. 46, no. 11, pp. 1964–1975, 1998.

[8] S. V. Hum and J. Perruisseau-Carrier, "Reconfigurable reflectarrays and array lenses for dynamic antenna beam control: A review," *IEEE Transactions on Antennas and Propagation*, vol. 62, no. 1, pp. 183–198, 2014.

[9] N. Misran, R. Cahill, and V. F. Fusco, "RCS reduction technique for reflectarray antennas," *Electronics Letters*, vol. 39, pp. 1630–2–, Nov 2003.

[10] B. A. Munk, *Frequency Selective Surfaces: Theory and Design*. New York: John Wiley and Sons, 2000.

[11] I. Anderson, "On the theory of self-resonant grids," *The Bell System Technical Journal*, vol. 54, pp. 1725–1731, Dec. 1975.

[12] C.-H. Tsao and R. Mittra, "Spectral-domain analysis of frequency selective surfaces comprised of periodic arrays of cross dipoles and jerusalem crosses," *IEEE Transactions on Antennas and Propagation*, vol. 32, pp. 478–486, May 1984.

[13] V. S. Asadchy, A. Díaz-Rubio, and S. A. Tretyakov, "Bianisotropic metasurfaces: physics and applications," *Nanophotonics*, vol. 7, no. 6, pp. 1069–1094, 2018.

[14] C. L. Holloway, E. F. Kuester, J. A. Gordon, J. O'Hara, J. Booth, and D. R. Smith, "An overview of the theory and applications of metasurfaces: The two-dimensional equivalents of metamaterials," *IEEE Antennas and Propagation Magazine*, vol. 54, pp. 10–35, Apr. 2012.

[15] S. B. Glybovski, S. A. Tretyakov, P. A. Belov, Y. S. Kivshar, and C. R. Simovski, "Metasurfaces: From microwaves to visible," *Physics Reports*, vol. 634, pp. 1–72, May 2016.

[16] H.-T. Chen, A. J. Taylor, and N. Yu, "A review of metasurfaces: Physics and applications," *Reports on Progress in Physics*, vol. 79, no. 7, p. 076401, 2016.

[17] A. E. Krasnok, A. E. Miroshnichenko, P. A. Belov, and Y. S. Kivshar, "Huygens optical elements and yagi—uda nanoantennas based on dielectric nanoparticles," *JETP Letters*, vol. 94, pp. 593–598, Dec 2011.

[18] J. M. Geffrin, B. García-Cámara, R. Gómez-Medina, P. Albella, L. S. Froufe-Pérez, C. Eyraud, A. Litman, R. Vaillon, F. González, M. Nieto-Vesperinas, J. J. Sáenz, and F. Moreno, "Magnetic and electric coherence in forward- and back-scattered electromagnetic waves by a single dielectric subwavelength sphere," *Nature Communications*, vol. 3, p. 1171, Nov. 2012.

[19] M. Selvanayagam and G. V. Eleftheriades, "Circuit modeling of Huygens surfaces," *IEEE Antennas and Wireless Propagation Letters*, vol. 12, pp. 1642–1645, 2013.

[20] C. Pfeiffer and A. Grbic, "Metamaterial Huygens' surfaces: Tailoring wave fronts with reflectionless sheets," *Physical Review Letters*, vol. 110, p. 197401, May 2013.

[21] F. Monticone, N. M. Estakhri, and A. Alù, "Full control of nanoscale optical transmission with a composite metascreen," *Physical Review Letters*, vol. 110, p. 203903, May 2013.

[22] A. Epstein and G. V. Eleftheriades, "Huygens' metasurfaces via the equivalence principle: Design and applications," *JOSA B*, vol. 33, pp. A31–A50, Feb. 2016.

[23] V. S. Asadchy, I. A. Faniayeu, Y. Ra'di, S. A. Khakhomov, I. V. Semchenko, and S. A. Tretyakov, "Broadband reflectionless metasheets: Frequency-selective transmission and perfect absorption," *Physical Review X*, vol. 5, p. 031005, July 2015.

[24] A. A. Elsakka, V. S. Asadchy, I. A. Faniayeu, S. N. Tcvetkova, and S. A. Tretyakov, "Multifunctional cascaded metamaterials: Integrated transmitarrays," *IEEE Transactions on Antennas and Propagation*, vol. 64, pp. 4266–4276, Oct. 2016.

[25] A. H. Dorrah and G. V. Eleftheriades, "All-pass characteristics of a huygens' unit cell," in *2018 United States National Committee of URSI National Radio Science Meeting (USNC-URSI NRSM)*, pp. 1–2, Jan 2018.

[26] T. Niemi, A. O. Karilainen, and S. A. Tretyakov, "Synthesis of polarization transformers," *IEEE Transactions on Antennas and Propagation*, vol. 61, pp. 3102–3111, June 2013.

[27] V. S. Asadchy, Y. Ra'di, J. Vehmas, and S. A. Tretyakov, "Functional metamirrors using bianisotropic elements," *Physical Review Letters*, vol. 114, p. 095503, Mar. 2015.

[28] I. Faniayeu, S. Khakhomov, I. Semchenko, and V. Mizeikis, "Highly transparent twist polarizer metasurface," *Applied Physics Letters*, vol. 111, no. 11, p. 111108, 2017.

[29] R. S. Khandpur, *Printed circuit boards: design, fabrication, assembly and testing*. Tata McGraw-Hill Education, 2005.

[30] B. Wang, J. Zhou, T. Koschny, M. Kafesaki, and C. M. Soukoulis, "Chiral metamaterials: simulations and experiments," *Journal of Optics A: Pure and Applied Optics*, vol. 11, no. 11, p. 114003, 2009.

[31] M. Li, L. Guo, J. Dong, and H. Yang, "An ultra-thin chiral metamaterial absorber with high selectivity for LCP and RCP waves," *Journal of Physics D: Applied Physics*, vol. 47, no. 18, p. 185102, 2014.

[32] J. P. S. Wong, M. Selvanayagam, and G. V. Eleftheriades, "Design of unit cells and demonstration of methods for synthesizing Huygens metasurfaces," *Photonics and Nanostructures - Fundamentals and Applications*, vol. 12, pp. 360–375, Aug. 2014.

[33] N. I. Landy, C. M. Bingham, T. Tyler, N. Jokerst, D. R. Smith, and W. J. Padilla, "Design, theory, and measurement of a polarization-insensitive absorber for terahertz imaging," *Physical Review B*, vol. 79, p. 125104, Mar. 2009.

[34] R. Paniagua-Domínguez, F. López-Tejeira, R. Marqués, and J. A. Sánchez-Gil, "Metallo-dielectric core-shell nanospheres as building blocks for optical three-dimensional isotropic negative-index metamaterials," *New Journal of Physics*, vol. 13, no. 12, p. 123017, 2011.

[35] D. Morits and C. Simovski, "Isotropic negative refractive index at near infrared," *Journal of Optics*, vol. 14, no. 12, p. 125102, 2012.

[36] Y. Ra'di, V. S. Asadchy, S. U. Kosulnikov, M. M. Omelyanovich, D. Morits, A. V. Osipov, C. R. Simovski, and S. A. Tretyakov, "Full light absorption in single arrays of spherical nanoparticles," *ACS Photonics*, vol. 2, no. 5, pp. 653–660, 2015.

[37] S. Campione, L. I. Basilio, L. K. Warne, and M. B. Sinclair, "Tailoring dielectric resonator geometries for directional scattering and Huygens' metasurfaces," *Optics Express*, vol. 23, pp. 2293–2307, Feb. 2015.

[38] A. Serdyukov, I. Semchenko, S. Tretyakov, and A. Sihvola, *Electromagnetics of Bi-Anisotropic Materials - Theory and Application*, vol. 11. Amsterdam: Gordon and Breach Science Publishers, 2001.

[39] I. V. Semchenko, S. A. Khakhomov, and A. L. Samofalov, "Helices of optimal shape for nonreflecting covering," *The European Physical Journal Applied Physics*, vol. 49, p. 33002, Mar. 2010.

[40] A. Balmakou, M. Podalov, S. Khakhomov, D. Stavenga, and I. Semchenko, "Ground-plane-less bidirectional terahertz absorber based on omega resonators," *Optics Letters*, vol. 40, pp. 2084–2087, May 2015.

[41] J. D. Baena and M. Londoño, "Broadband transparent metasurfaces for full phase shift and polarization control," in *2016 10th International Congress on Advanced Electromagnetic Materials in Microwaves and Optics (METAMATERIALS)*, pp. 43–45, Sept 2016.

[42] M. Londono, A. Sayanskiy, J. L. Araque-Quijano, S. B. Glybovski, and J. D. Baena, "Broadband Huygens' metasurface based on hybrid resonances," *arXiv:1804.07806 [physics]*, Apr. 2018. arXiv: 1804.07806.

[43] S. A. Tretyakov, F. Mariotte, C. R. Simovski, T. G. Kharina, and J. P. Heliot, "Analytical antenna model for chiral scatterers: Comparison with numerical and experimental data," *IEEE Transactions on Antennas and Propagation*, vol. 44, pp. 1006–1014, July 1996.

[44] V. S. Asadchy, I. A. Faniayeu, Y. Ra'di, and S. A. Tretyakov, "Determining polarizability tensors for an arbitrary small electromagnetic scatterer," *Photonics and Nanostructures - Fundamentals and Applications*, vol. 12, pp. 298–304, Aug. 2014.

[45] Y. Ra'di, V. S. Asadchy, and S. A. Tretyakov, "Tailoring reflections from thin composite metamirrors," *IEEE Transactions on Antennas and Propagation*, vol. 62, pp. 3749–3760, July 2014.

[46] Y. Ra'di, V. S. Asadchy, and S. A. Tretyakov, "Total absorption of electromagnetic waves in ultimately thin layers," *IEEE Transactions on Antennas and Propagation*, vol. 61, pp. 4606–4614, Sept. 2013.

[47] S. Tretyakov, *Analytical Modeling in Applied Electromagnetics*. Boston: Artech House, 2003.

[48] "ANSYS HFSS [online]. Available: http://www.ansys.com/products/electronics/ansys-hfss," 2014.

[49] A. V. Osipov and S. A. Tretyakov, *Modern Electromagnetic Scattering Theory with Applications*. John Wiley & Sons, 2017.

[50] N. Amitay and A. A. M. Saleh, "Broad-band wide-angle quasi-optical polarization rotators," *IEEE Transactions on Antennas and Propagation*, vol. 31, pp. 73–76, Jan. 1983.

[51] L. Cong, W. Cao, X. Zhang, Z. Tian, J. Gu, R. Singh, J. Han, and W. Zhang, "A perfect metamaterial polarization rotator," *Applied Physics Letters*, vol. 103, p. 171107, Oct. 2013.

[52] L. Cong, W. Cao, Z. Tian, J. Gu, J. Han, and W. Zhang, "Manipulating polarization states of terahertz radiation using metamaterials," *New Journal of Physics*, vol. 14, no. 11, p. 115013, 2012.

[53] A. Shaltout, J. Liu, V. M. Shalaev, and A. V. Kildishev, "Optically active metasurface with non-chiral plasmonic nanoantennas," *Nano Letters*, vol. 14, pp. 4426–4431, Aug. 2014.

[54] S. I. Maslovski, D. K. Morits, and S. A. Tretyakov, "Symmetry and reciprocity constraints on diffraction by gratings of quasi-planar particles," *Journal of Optics A: Pure and Applied Optics*, vol. 11, no. 7, p. 074004, 2009.

[55] Y. Svirko, N. Zheludev, and M. Osipov, "Layered chiral metallic microstructures with inductive coupling," *Applied Physics Letters*, vol. 78, pp. 498–500, Jan. 2001.

[56] N. Kanda, K. Konishi, and M. Kuwata-Gonokami, "Terahertz wave polarization rotation with double layered metal grating of complimentary chiral patterns," *Opt. Express*, vol. 15, pp. 11117–11125, Sep 2007.

[57] M. Decker, R. Zhao, C. M. Soukoulis, S. Linden, and M. Wegener, "Twisted split-ring-resonator photonic metamaterial with huge optical activity," *Opt. Lett.*, vol. 35, pp. 1593–1595, May 2010.

[58] Y. Ye and S. He, "90° polarization rotator using a bilayered chiral metamaterial with giant optical activity," *Applied Physics Letters*, vol. 96, p. 203501, May 2010.

[59] J. J. David, *Electrodynamics*. Major Reference Works, Wiley-VCH Verlag GmbH & Co. KGaA, Sept. 1975.

[60] N. K. Grady, J. E. Heyes, D. R. Chowdhury, Y. Zeng, M. T. Reiten, A. K. Azad, A. J. Taylor, D. A. R. Dalvit, and H.-T. Chen, "Terahertz metamaterials for linear polarization conversion and anomalous refraction," *Science*, p. 1235399, May 2013.

[61] Y. Z. Cheng, W. Withayachumnankul, A. Upadhyay, D. Headland, Y. Nie, R. Z. Gong, M. Bhaskaran, S. Sriram, and D. Abbott, "Ultrabroadband reflective polarization convertor for terahertz waves," *Applied Physics Letters*, vol. 105, p. 181111, Nov. 2014.

[62] H. F. Ma, G. Z. Wang, G. S. Kong, and T. J. Cui, "Broadband circular and linear polarization conversions realized by thin birefringent reflective metasurfaces," *Optical Materials Express*, vol. 4, pp. 1717–1724, Aug. 2014.

[63] E. Plum and N. I. Zheludev, "Chiral mirrors," *Applied Physics Letters*, vol. 106, no. 22, p. 221901, 2015.

[64] N. Yu, P. Genevet, M. A. Kats, F. Aieta, J.-P. Tetienne, F. Capasso, and Z. Gaburro, "Light propagation with phase discontinuities: Generalized laws of reflection and refraction," *Science*, vol. 334, pp. 333–337, Oct. 2011.

[65] J. P. S. Wong, A. Epstein, and G. V. Eleftheriades, "Reflectionless wide-angle refracting metasurfaces," *IEEE Antennas and Wireless Propagation Letters*, vol. 15, pp. 1293–1296, 2016.

[66] V. S. Asadchy, M. Albooyeh, S. N. Tcvetkova, A. Díaz-Rubio, Y. Ra'di, and S. A. Tretyakov, "Perfect control of reflection and refraction using spatially dispersive metasurfaces," *Physical Review B*, vol. 94, p. 075142, Aug. 2016.

[67] A. Díaz-Rubio, V. Asadchy, A. Elsakka, and S. Tretyakov, "From the generalized reflection law to the realization of perfect anomalous reflectors," *Science Advances*, vol. 3, p. e1602714, Aug. 2017.

[68] M. Chen, E. Abdo-Sánchez, A. Epstein, and G. V. Eleftheriades, "Theory, design, and experimental verification of a reflectionless bianisotropic huygens' metasurface for wide-angle refraction," *Phys. Rev. B*, vol. 97, p. 125433, Mar 2018.

[69] G. Lavigne, K. Achouri, V. S. Asadchy, S. A. Tretyakov, and C. Caloz, "Susceptibility derivation and experimental demonstration of refracting metasurfaces without spurious diffraction," *IEEE Transactions on Antennas and Propagation*, vol. 66, pp. 1321–1330, March 2018.